

Sulfurization of co-evaporated $\text{Cu}_2\text{ZnGeSe}_4$ layers: Influence of the precursor cation's ratios on the properties of $\text{Cu}_2\text{ZnGe}(\text{S,Se})_4$ thin films

David Palma-Lafuente^{a,*}, Pablo Diez-Silva^a, Victoria Rotaru^b, Tariq Jawhari^c, Tobias Bertram^d, Pablo Reyes-Figueroa^d, Maxim Guc^b, José Manuel Merino^a, Raquel Caballero^{a,**}

^a Universidad Autónoma de Madrid, Departamento de Física Aplicada, C/ Tomás y Valiente 7, 28049, Madrid, Spain

^b IREC, Catalonia Institute for Energy Research, C/ Jardins de Les Dones de Negre 1, Sant Adrià Del Besòs, 08930, Barcelona, Spain

^c CCiT, Universitat de Barcelona, Lluís Solé I Sabaris, 1-3, 08028, Barcelona, Spain

^d PVcomB, Helmholtz Zentrum Berlin für Materialien und Energie, Schwarzschildstrasse 3, Berlin, 12489, Germany

ARTICLE INFO

Keywords:

Kesterite

$\text{Cu}_2\text{ZnGe}(\text{S,Se})_4$

Sulfurization

Break-off experiments

Thin films

ABSTRACT

$\text{Cu}_2\text{ZnGe}(\text{S,Se})_4$ (CZGSSe) thin films were fabricated by sulfurization of co-evaporated $\text{Cu}_2\text{ZnGeSe}_4$ (CZGSe) thin films. The goal of this work is to investigate the effect of the composition of CZGSe layers on the structural, vibrational and morphological properties of CZGSSe compounds. Different CZGSe layers with different cation's ratios (Cu-poor, Zn-rich; Cu-poor, Zn-stoichiometric and Cu-poor, Ge-rich) were investigated before and after the sulfurization process. Break-off and different cooling experiments during sulfurization of CZGSe were also carried out. Break-off experiments revealed that 440 °C is the key temperature to incorporate S into CZGSe lattice, being required 480 °C to enhance the interdiffusion of the elements. Fast cooling experiments during sulfurization appeared to be a promising strategy to avoid the formation of secondary phases. All the samples showed the CZGSSe kesterite phase, as well as higher S content and different secondary phases at the surface. These experiments demonstrate that a minimum Ge content in CZGSe is required to assist the growth of CZGSSe grains and develop a compact structure. These results indicate the importance of controlling the cation's ratio of CZGSe to develop high quality wide band gap CZGSSe compounds, which can be very attractive for different applications.

1. Introduction

$\text{Cu}_2\text{ZnSn}(\text{S,Se})_4$ -kesterite type material was shown to be a promising absorber for thin-film solar cells, achieving an efficiency of 13.6% [1]. This material which is formed by elements abundant in the Earth's crust and of low toxicity, presents a p-type conductivity and a high absorption coefficient $\sim 10^4 \text{ cm}^{-1}$ in the visible range. However, the device performance is still very far away from that obtained by $\text{Cu}(\text{In,Ga})\text{Se}_2$ and CdTe solar cells with 23.4% and 22.1% respectively [2]. The main limitation of kesterite technology is the open circuit voltage V_{OC} deficit, defined as $E_g/q - V_{\text{OC}}$, where E_g is the band gap energy and q is the electron charge, or in many studies as $V_{\text{OC}}\text{-SQ}$ deficit defined by the V_{OC} difference respect to the Shockley-Queisser limit. Many reasons were proposed to explain this deficit, as for example, the presence of secondary phases, the formation of deep defects, band gap potential fluctuations, short minority carrier lifetimes, interface recombination, etc.

[3,4]. The partial substitution of Sn with Ge showed an enhanced V_{OC} [5]; however, the increase of Ge led to a reduced device performance and the formation of deep defects [6,7]. Nevertheless, Choubac et al. [8] demonstrated that the total substitution of Sn with Ge, $\text{Cu}_2\text{ZnGeSe}_4$ (CZGSe), is a successful strategy to improve the V_{OC} of kesterite-based solar cells, achieving an efficiency of 8.5% for E_g near 1.4 eV. The band gap energy of this material can be modified by the substitution of Se with S, varying from 1.4 eV (CZGSe) to around 2.2 eV ($\text{Cu}_2\text{ZnGeS}_4$, CZGS) [9,10]. This range of E_g allows to open new market opportunities, as for example, Ge-pure kesterite material can be used for semi-transparent solar cells or as top cell of an efficient tandem device. For that, it is necessary to achieve E_g of 1.5 eV at least. In a previous work [11], we reported the first semi-transparent CZGSe-based solar cells with 5.8% efficiency (active area) and $E_g = 1.47 \text{ eV}$. The incorporation of S into the CZGSe lattice has led not only to an increase in E_g , but also to a larger V_{OC} deficit [12,13]. Therefore, the fabrication of

* Corresponding author.

** Corresponding author.

E-mail addresses: david.palma@uam.es (D. Palma-Lafuente), raquel.caballero@uam.es (R. Caballero).

wide band gap kesterite is a challenge to improve the device efficiency. However, there are not a lot of studies about wide band gap of pure Ge-kesterite material and solar cells in comparison with their Sn counterpart. Gunder et al. [14] revealed the existence of different defects in off-stoichiometric kesterite-type CZGSe powder samples, such as copper vacancies V_{Cu} , various cation antisite defects (Cu_{Zn} , Zn_{Cu} , Zn_{Ge} , Cu_{Ge}) as well as interstitials (Cu_i , Zn_i). The Cu_{Ge} defect, which is very detrimental for the optoelectronic properties, exists only in Cu-rich CZGSe conditions. In addition, they showed an increase in the E_g of CZGSe with decreasing $[Cu]/([Zn]+[Ge])$ atomic ratio [14]. More recently, Ratz et al. [15] studied the Ge-related defects in CZGS by first-principles calculations. They identified Ge_{Zn} as recombination centre, which presents higher formation energy than that of V_{Cu} , Cu_{Zn} and Zn_{Cu} defects. But the distortion of the lattice induced by Ge_{Zn} defect is reduced in comparison to its Sn_{Zn} counterpart, being less detrimental with a reduction of non-radiative recombination rate that could explain the V_{OC} improvement by Ge incorporation. Schnabel et al. [13,16,17] studied the incorporation of S into solution-processed CZGSSe layers by the variation of the GeS amount added during the annealing step at high temperature, achieving CZGSSe-based PV devices with $\eta = 2.1\%$ and 6.0% for $E_g = 1.54$ eV and 1.47 eV respectively. Courel et al. [18] fabricated one of the first CZGS thin films by evaporation, that could tailor the band gap of the semiconductor in the range of 2.00 – 2.23 eV by varying Ge concentration. More recently, we already achieved a promising performance of 3.2% for CZGSSe-based devices with $E_g = 1.98$ eV by the sulfurization of co-evaporated CZGSe and controlling the incorporation method of a NaF layer that affects the $[S]/([S]+[Se])$ gradient [12]. It is well known that the control of the $[S]/([S]+[Se])$ distribution through the kesterite layer is important to enhance the photovoltaic parameters [4,12,19,20]; but the difficulty of creating the proper gradient with a higher S concentration at the surface is also well known [21]. It is of prime importance to identify the key parameters during the growth of the thin films that enhance the properties of the CZGSSe compound to produce high efficiency solar cells. It is known that a Cu-poor and Zn-rich composition is necessary to achieve high efficiency kesterite-based solar cells. However, as mentioned before, the formation of secondary phases can be very detrimental for the PV device [22], being very important the control of the cation atomic ratios of the absorber layer.

In this work, CZGSSe thin films were grown by sulfurization of CZGSe co-evaporated onto Mo/soda-lime glass (SLG) substrates. The growth of CZGSSe thin films was first studied by different break-off experiments during the sulfurization process. The goal of this work is to investigate the influence of the CZGSe composition on the structural, vibrational and morphological properties of the final CZGSSe compound. The importance of controlling the cation ratios of CZGSe grown at low temperature to produce a good quality CZGSSe material is demonstrated here. This study is critical to understand and control the incorporation of S into the CZGSe lattice, which is fundamental to increase both E_g and solar cells performance. These results can be translated to the fabrication of semi-transparent devices to expand the range of applications.

2. Materials and methods

2.1. $Cu_2ZnGe(S,Se)_4$ thin films growth process

$Cu_2ZnGeSe_4$ thin films were fabricated by co-evaporation of Cu, ZnSe, Ge and Se onto Mo/SLG substrates at a nominal substrate temperature of 150°C [12,20]. This low temperature was chosen in order to reduce the re-evaporation of Ge and Se. The co-evaporation process consisted of 3 stages. During the first stage, Cu, ZnSe, Ge and Se were evaporated to obtain a Cu-rich composition to assist the formation of kesterite-type crystals. In the second stage, ZnSe, Ge and Se were deposited to achieve a final Cu-poor composition. Finally, in the third stage, Ge and Se were evaporated to avoid a Zn excess on the surface [12,

20]. Due to the low substrate temperature used during co-evaporation process and the beneficial effect of Na on kesterite absorber layers [23], a NaF precursor layer of a nominal thickness of 6 nm was evaporated at a substrate temperature of around 35°C before the co-evaporation process in the same vacuum chamber. Therefore, the Na present in the kesterite-type material is coming from the NaF layer and the diffusion from the SLG substrate. Different co-evaporation processes were carried out to investigate the effect of the composition of the CZGSe thin films on the formation of CZGSSe compound. The different concentrations of the cations were regulated by modifying the evaporation rates of Cu and/or Zn. Table 1 shows the different processes 1, 2, 3 and 4 with different cation ratios. The Mo back contact was deposited by DC sputtering in a Leybold Optics A600V7 P379 tool under high vacuum conditions, using a dynamic deposition process, i.e. the substrate is oscillating in front of a Mo target (99.95%) at a speed of ~ 0.5 m/min. The nominal targeted thickness of the Mo back contact was 800 nm.

The co-evaporation procedure was followed by a sulfurization process in a tubular furnace in Ar atmosphere. The samples were placed into a graphite box, along with 22 mg of S and 6 mg of GeS to incorporate S into the material [20]. In order to understand the growth kinetic of CZGSSe, different break-off experiments were performed during the sulfurization process: the sulfurization procedure was interrupted at different temperatures (350° , 400° , 440° and 480°C) for the CZGSe thin films coming from the first co-evaporation process (see Table 1). The break-off experiments were carried out by removing the samples from the hot zone of the furnace by means of a transfer bar. Fig. 1 shows a scheme of the break-off experiments performed during the sulfurization process. After that, the sulfurization at 480°C for 60 min, at a pressure of around 950 mbar with a heating rate of $20^\circ\text{C}/\text{min}$, and cooling rate of $10^\circ\text{C}/\text{min}$ was considered as the standard process and was therefore used to investigate the influence of the CZGSe composition on the CZGSSe properties in the case of co-evaporation 2, 3 and 4 as shown in Table 1. The effect of the cooling rate during the thermal treatment and the time at the maximum temperature, i.e. co-evaporation 4, was finally studied. The conditions of the sulfurization processes can be found in Table 1.

CZGSSe thin films were grown with thicknesses ≤ 1 μm and at maximum temperature of 480°C because these are the optimal conditions to increase the straight-through transmittance, as shown elsewhere [11]. By this way, these results are easier to translate for the fabrication of wide band gap kesterite on transparent substrates.

2.2. Sample characterization

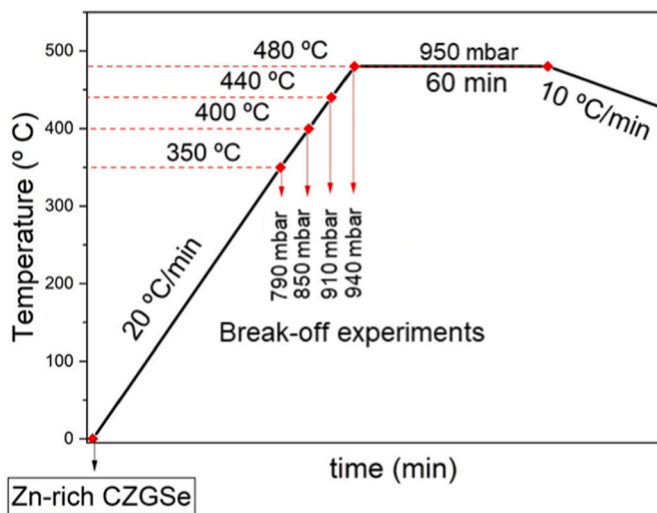
The chemical composition of the samples was measured by energy dispersive X-ray spectroscopy (EDX) using an Oxford INCAx-sight detector connected to a Hitachi S-3000 N scanning electron microscope (SEM). Bulk measurements were carried out at 25 kV operating voltage. Cu K, Zn K, Ge K, Se K and S K lines were used for elemental quantification. Additionally, elemental EDX mapping was performed at a lower operating voltage of 5 kV using an Octane Plus detector connected to a SEM FEI VERIOS 460 SEM. The morphology of the CZGSSe/Mo structure and the CZGSSe surface was investigated by using the last SEM system described above operating at 2 kV. Glow discharge optical emission spectrometry (GD-OES) was used to measure the in-depth element distribution through the CZGSSe thin-film. The measurements were obtained with a Spectrumba GDA 650 spectrometer with Argon plasma in a pulsed RF mode for sputtering and a CCD-array for the optical detection. The measurements are shown in arbitrary units since they were performed without a calibration sample (Kodalle et al., 2019). Grazing incidence X-ray diffraction (GIXRD) was measured using a PANalytical X'Pert Pro MPD diffractometer, with CuK_α radiation and a multilayer mirror to produce a parallel beam. The measurements were performed at incidence angle of 4° . The references patterns for phase identification were taken from the International Centre for Diffraction Data. Raman scattering spectra were measured using the monochromator FHR 640

Table 1

Description of the growth processes and composition of all the samples measured by EDX.

Exp.	T (°C)	Cu (at %)	Zn (at %)	Ge (at %)	S (at %)	Se (at %)	[Cu]/[Zn]+[Ge]	[Zn]/[Ge]	[S]/([S]+[Se])
Coev.1	–	20.2	15.4	7.7	–	56.7	0.87	2.00	–
bo	350	19.3	15.4	7.6	12.3	45.2	0.84	2.03	0.21
bo	400	19.8	15.5	7.7	23.1	33.8	0.86	2.01	0.41
bo	440	20.8	16.5	8.1	43.5	11.0	0.84	2.03	0.80
bo	480	20.6	16.1	8.1	40.3	14.9	0.85	1.98	0.73
60 min	480	18.4	14.1	11.0	45.9	10.7	0.74	1.29	0.81
Coev. 2	–	21.3	12.3	11.9	–	54.6	0.88	1.04	–
60 min	480	19.6	11.5	14.9	16.9	37.2	0.74	0.77	0.31
Coev. 3	–	16.7	12.1	12.4	–	58.8	0.68	0.98	–
60 min	480	15.1	11.2	12.2	39.0	22.5	0.64	0.92	0.63
Coev. 4	–	16.2	13.0	19.9	–	50.9	0.49	0.66	–
30 min-bo	480	17.3	13.2	11.2	23.6	34.6	0.71	1.18	0.40
30 min	480	16.9	13.5	11.5	21.1	37.1	0.68	1.17	0.36
60 min	480	17.2	13.5	11.6	20.1	37.5	0.68	1.17	0.35

Note: bo = break-off experiments.

**Fig. 1.** Scheme of the break-off experiments carried out during the sulfurization process as well as the temperature profile of the standard sulfurization route.

from Horiba Jobin Yvon coupled with a CCD detector. The spectra were measured in backscattering configuration using a special probe designed at IREC. The HeCd gas laser (325 nm, ~90 W/cm² and 442 nm, ~90 W/cm²) and YAG:Nd solid state laser (532 nm, ~100 W/cm²) were used as excitation sources. Spectral position was corrected by imposing the main peak of single crystalline Si to 520 cm⁻¹.

In-depth micro-Raman spectra were obtained using a LabRam HR 800 spectrometer coupled to an optical microscope Olympus BXM with a dispersive grating of 600 g/mm and a CCD detector cooled at -65 °C using as an excitation source a 532 nm solid-state laser. The laser power at the sample was fixed at 0.05 mW in order to avoid thermal effects with a 100× microscope objective (~1.5 kW/cm²). In order to get an in-depth Raman study of the absorber layer, the samples were prepared as follows: The back layer of SLG was first manually polished to get a total sample thickness between 150 and 350 μm. Further thinning was carried out using a low angle ion milling machine (Model 1010 Low Angle Ion Mill Fischione Instrument). An argon ion source with 5 kV voltage and 5 mA current was used to thin the sample at 7° angle.

3. Results and discussion

3.1. Sulfurization process of Zn-rich CZGSe thin films

The atomic composition measured by EDX of each sample corresponding to the different break-off experiments made at different temperatures during the sulfurization process is shown in Table 1. These samples are coming from the co-evaporation process 1 with a very Zn-rich and Cu-poor composition. It can here be observed that the S content clearly rises as the temperature is increased up to 440 °C. However, a significant increase in Ge content and Zn loss can be seen when maintaining the temperature at 480 °C for 60 min which allows to get a final optimal composition, Cu-poor and Zn-rich with [Zn]/[Ge] = 1.29, to produce efficient solar cells as already shown elsewhere [8,12]. The main reason for working with Zn-rich composition is to avoid the formation of Ge_{Zn} antisite deep defect [15], which is detrimental for the solar cell.

GD-OES measurements were performed to investigate the elements distribution through the kesterite-type material in all the experiments. Fig. 2 shows the elements depth profile corresponding to the samples of the Process 1. It should be mentioned that the steep gradient observed for the element's signals at the surface of the thin films during the first seconds of the measurement, seems to be an artifact induced by the sputter process (dashed line in Fig. 2). As explained in the Experimental section, the CZGSe co-evaporation process was finished with the evaporation of only Ge and Se after 7.5 min, explaining the higher Ge and Se contents and lower Zn concentration at the surface of the co-evaporated thin film (see Fig. 2a.). The higher Cu content observed near the back contact is explained by the evaporation of Cu-rich ratio of elements during the first stage of the growth process. This indicates that the substrate temperature of 150 °C is very low to enhance the interdiffusion of the elements. This fact is also corroborated by the Na-signal, which is only detected at the back interface and at the back contact. It is also interesting to observe that Se and Ge-depth have similar depth profiles, whereas Cu shows an opposite evolution. The local minimum of the Cu-signal coincides with the maximum of the Ge-signal which could suggest the formation of Ge_{Cu} antisite defects, similar to what happens for Cu₂ZnSnSe₂ with the formation of Sn_{Cu} defects, or Ge-Se secondary phase formation, both being negative for the device performance [6,11]. However, such Ge_{Cu} defects would be expected for Ge-rich composition [14]. This behaviour is observed up to 400 °C and can be related to the low temperature used. The interruption of the sulfurization process at 350 °C shows the incorporation of S through the thin film, specially accumulated at the surface region, as well as the interdiffusion process of the rest of the elements that starts to take place (see Fig. 2b.).

The results show a significant high Cu content near the surface for the experiments interrupted at 350, 400 and 440 °C (Fig. 2b and d)

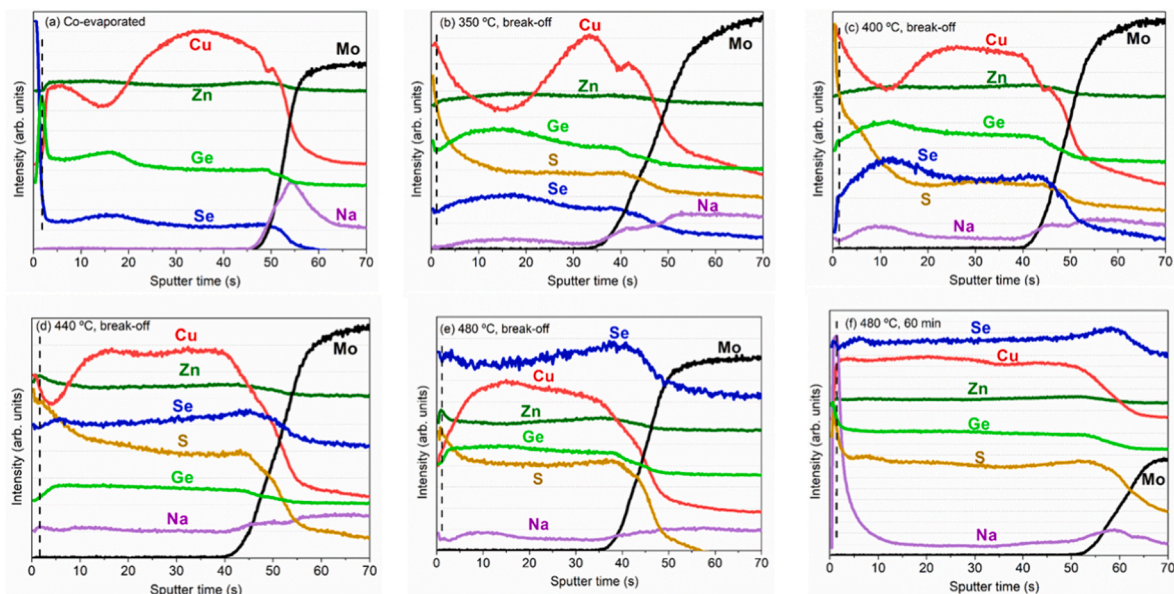


Fig. 2. GD-OES depth profiles of CZG(S)Se/Mo structure for all the samples corresponding to the Process 1.

which seem to indicate that Cu accumulated near the Mo layer for the CZGSe thin film diffuses towards the surface as the sulfurization temperature increases. In contrast, the Cu concentration is found to be lower at the surface when the temperature achieves 480 °C (Fig. 2e and f). A lower Cu content at the surface region of the absorber layer is beneficial to increase the device efficiency. A slightly higher Zn-signal is detected at the surface for the samples sulfurized at temperatures ≥ 400 °C. A more uniform distribution of the elements takes place when the samples are treated at the highest temperature, i.e. 480 °C for 60 min, and this coincides with the desired $[Zn]/[Ge]$ atomic ratio. It is essential to highlight the importance of the dwell time at the highest temperature, necessary for the elements redistribution and Na diffusion towards the surface of the kesterite layer. In any case, all the samples treated under elemental S and GeS are characterized by a higher S content near the surface. The depth profiles also show that the Se and S distributions exhibit opposite tendencies, which confirms that S atoms substitute Se atoms. Fig. 3a. Shows the normalized $[S]/([S]+[Se])$ atomic ratio gradient through the kesterite layer. 440 °C is clearly the key temperature, in which a higher S content is incorporated and a different and larger single $[S]/([S]+[Se])$ gradient starts to be developed with a more pronounced increase of the atomic ratio at the surface. The importance of the S accumulation at the surface region of kesterite in enhancing the V_{OC} of the solar cell device is known [19,20]. We already reported a $[S]/([S]+[Se])$ -gradient through CZGSSe thin films with a higher ratio at the surface and decreasing towards the back contact, where the S distribution was controlled by the NaF precursor layer thickness [20] as well as by the incorporation method of the NaF film [12]. We also

showed that Na promotes the partial substitution of Se with S, replacing the possible Se vacancies by S, increasing the band gap energy of kesterite-type material [20,25]. As shown in Fig. 2, the increase of annealing temperature leads to a higher Na content near the surface of CZGSSe, corresponding with the region with higher S concentration. Simulations of the optimum band gap grading profile of CZTSSe [25] concluded that a graded band gap results in higher performances than a flat distribution of $[S]/([S]+[Se])$ because of an increase of the carrier collection. In our study, no flat distribution of S was observed.

Elemental EDX mapping of the surface of the different samples was performed, as shown in Fig. 4. Formation of different grains was observed, which correspond to different phases. A high amount of Se and regions with high Ge and Zn content, where Cu was not detected, can be observed in the elemental EDX map of the co-evaporated CZGSe sample which is in agreement with the GD-OES signal of the sample surface. Once the sulfurization process starts, Se content begins to decrease and bigger grains corresponding to Cu-S-Se are formed, being more significant until 440 °C. At around 440–480 °C higher Zn content is also detected, in agreement with the Zn- GD-OES signal. However, the sulfurization at the maximum temperature for 60 min leads to a much more uniform distribution of all the elements that constitute the kesterite compound. These results are in good agreement with the GD-OES measurements.

GIXRD diffractograms of the samples corresponding to Process 1 are displayed in Fig. 5. The co-evaporated sample is characterized by the presence of CZGSe phase (01-070-7623) with the identification of the main 112, 220, 204, 312 and 116 Bragg reflections with a low

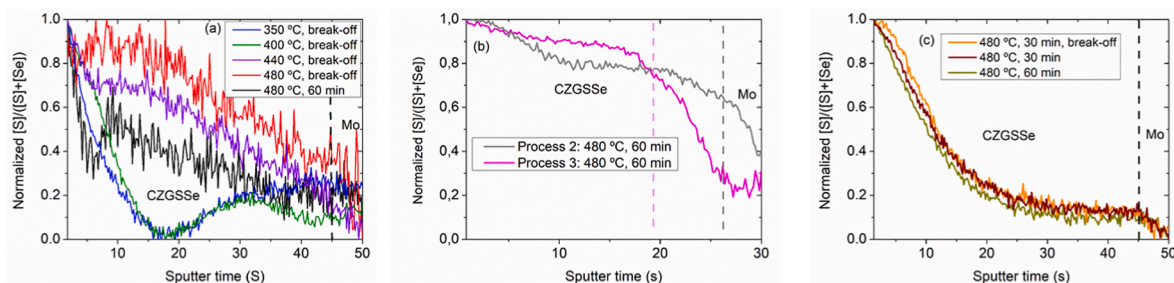


Fig. 3. GD-OES depth profiles of the normalized $[S]/([S]+[Se])$ atomic ratio for all the sulfurized samples corresponding to (a) Process 1, (b) Processes 2 and 3, and (c) Process 4.

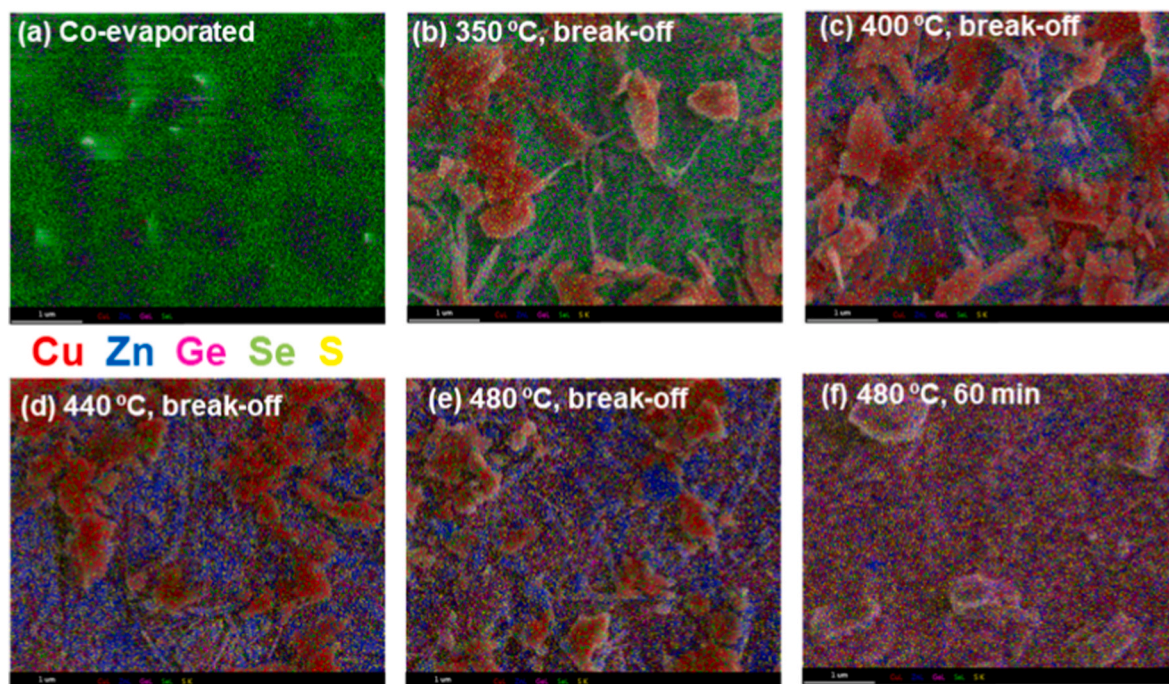


Fig. 4. Elemental EDX mapping of all the samples corresponding to the Process 1.

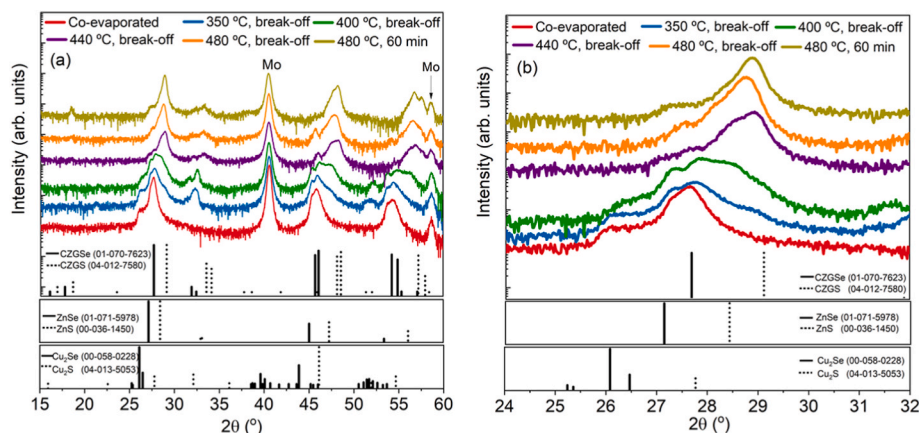


Fig. 5. GIXRD patterns measured of all the samples investigated corresponding to Process 1.

crystallinity due to the low growth temperature used. Mo Bragg reflections (04-014-7439) corresponding to the back contact was also identified. A diffraction peak was observed at around 26° that could correspond to Cu_2Se phase, which disappears when the annealing temperature is higher than 350°C . The presence of ZnSe and Cu_2GeSe_3 secondary phases cannot be discarded because of the proximity of their diffraction peaks with those of the kesterite phase. Once the sulfurization starts, CZGSSe phases can be identified with the Bragg peaks position situated between CZGS (04-012-7580) and CZGSe . A shift towards higher diffraction angles is observed when increasing the sulfurization temperature, corroborating the higher amount of S incorporated into the lattice. In addition, the presence and formation of ZnS and/or Zn(S,Se) phases cannot be ruled out during the sulfurization process, in agreement with the Zn-rich composition. During the incorporation of S, a $\text{Cu}_2(\text{S,Se})$ secondary phase is segregated and only disappears when the sample is heated at the maximum temperature for the longer time in agreement with the elemental EDX mapping results. A clear contribution of two different peaks related to the existence of two phases with different $[\text{S}]/([\text{S}]+[\text{Se}])$ atomic ratios are detected from the sample

sulfurized at 400°C , being very significant at 440°C . Fig. 5b. Shows a plot of the region of the 112 Bragg peak of CZG(S)Se thin films, indicating the incorporation of S into the lattice as well as the clear presence of secondary phases. Finally, the 112 Bragg reflection peak of the samples annealed during 60 min at 480°C appears quite narrow with only a small asymmetry towards the lower angles and close to the position of pure CZGS . The former denotes good crystalline quality of the obtained thin film and a gentle change of the $[\text{S}]/([\text{S}]+[\text{Se}])$ ratio in accordance with GD-OES results, while the later correlates with the S-rich composition of this sample obtained from EDX.

In order to identify all phases potentially forming at different stages of the formation of CZGSSe compound, a multiwavelength Raman scattering analysis was carried out. We used UV and visible excitation wavelengths (332, 442 and 532 nm) to obtain information about the phase formation at the layer surface. 332 and 442 nm excitation wavelengths were used to examine the possible presence of ZnS and ZnSe secondary phases respectively, or their possible solid solutions. Note, that the spectra measured under 442 nm excitation wavelength are not presented here as they did not exhibited the presence of ZnSe

secondary phase and were similar to the spectra measured under 532 nm excitation wavelength. Fig. 6 plots the Raman scattering measurements of all the samples investigated using the different excitation wavelengths. The main Raman peaks of the co-evaporated sample can be attributed to pure Se phases (trigonal t-Se and amorphous a-Se [26], in agreement with the significant amount of Se detected by elemental EDX mapping (see Fig. 4a). The small vibrational modes at 194 and 142 cm^{-1} can be related to GeSe_2 [27] and/or Cu_2GeSe_3 [28] secondary phases, the former being more probable, due to the final evaporation stage where only Ge and Se atoms are evaporated. Thus, no Raman peaks of kesterite compound were found at the surface of this co-evaporated sample. Low annealing temperatures ($\leq 400^\circ\text{C}$) also do not result in the formation of the kesterite phase at the samples surface, as shown in Fig. 6a., and the main Raman peaks in the spectra of samples sulfurized at 350° and 400°C can be attributed to different secondary phases as GeS , Cu_2GeSe_3 , $\text{Zn}(\text{S,Se})$, etc. Annealing at the temperatures $\geq 440^\circ\text{C}$ results in the formation of the kesterite phase which becomes dominant. However, in all these samples there is a significant amount of ZnS secondary phase, very small for the sample treated during 60 min (see Fig. 6b measured under 325 nm excitation) and some amount of $\text{Ge}(\text{S,Se})_2$ secondary phase (see Fig. 6a measured under 532 nm excitation). Analysis of the Raman spectra measured in different points of each sample revealed a significant lateral inhomogeneity in terms of $[\text{S}]/([\text{S}]+[\text{Se}])$ ratio and in terms of the presence of secondary phase presence for all the samples, but it is significantly reduced for the sample annealed at 480°C for 60 min, indicating a greater uniformity of this sample surface, in agreement with elemental EDX mapping. Note, that the anions ratio was estimated from the Raman spectra by comparing the relative integrated intensities of the peaks related to Se-Se vibrations, S-Se vibrations and S-S vibrations, in agreement with previously published methodology proposed for CZGSSe [12,21] and for familiar $\text{Cu}_2\text{ZnSn}(\text{S,Se})_4$ solid solutions [29].

The phase analysis performed before shows some inconsistency between GIXRD and Raman results. GIXRD diffractograms show the presence of main diffraction peaks between the main Bragg reflections of CZGSe and CZGS phases, pointing to the formation of the kesterite phase in the bulk of the co-evaporated sample and also of the thin films annealed at low temperatures below or equal to 400°C , although unambiguous identification of the kesterite phase formation from the GIXRD data alone is rather complicated. On the other hand, Raman spectroscopy measurements do not show formation of the kesterite phase at the surface of the same samples. In order to clarify this inconsistency, in-depth Raman spectroscopy measurements have been performed for the co-evaporated sample, before the sulfurization treatment (Fig. 7). In accordance with the previous macro-Raman analysis, before the ion milling, the spectra exhibited mainly pure Se phases at the sample surface, and a strong difference between different measurement spot has been seen in terms of relative intensity of the peaks related to amorphous and trigonal Se phase. However, the spectra measured at the depth close to the front interface of the thin film shows a strong peak at

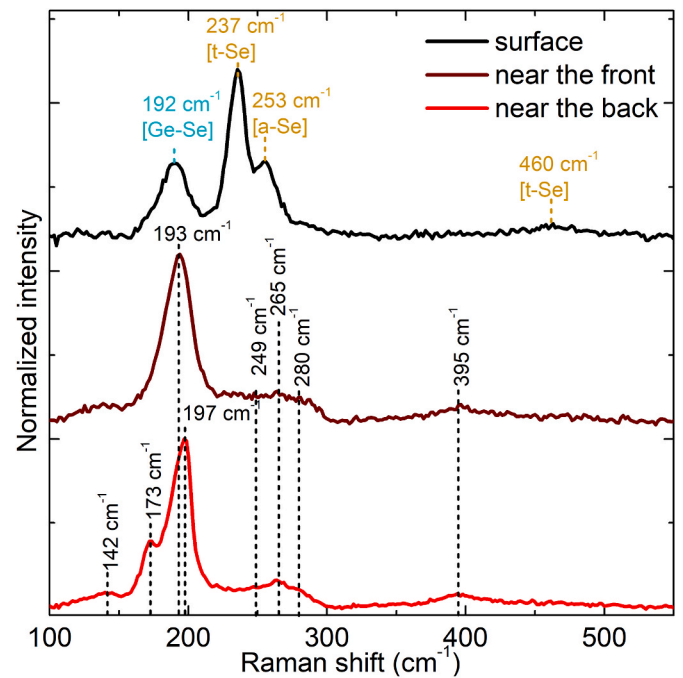


Fig. 7. Raman scattering spectra measured under 532 nm excitation in the co-evaporated sample before (black curve) and after (dark red and red curves) ion milling. Note that two curves after the ion milling correspond to different depth closer to front interface (dark red curve) and closer to the back interface (red curve).

198 cm^{-1} assigned to the CZGSe kesterite phase (see dark red curve in Fig. 7). This, however, appears to be quite broad denoting the low crystalline quality of the compound. No peaks of secondary phases can be already observed at this depth, resulting that pure Se phase is mainly collected at the samples surface. Going more in depth, the spectra of the kesterite phase becomes more pronounced with a decreased width of the main peak shifted to 202 cm^{-1} (see red curve in Fig. 7). In addition, several less intense peaks all attributed to CZGSe kesterite phase [30] become better visible. All these Raman features correlate with better crystalline quality of the films close to the back contact. Finally, these measurements confirmed the in-depth formation of kesterite phase even for the as co-evaporated CZGSe thin film, as detected by GIXRD measurements, and allowed to conclude about the improvement of the crystalline quality with depth, which is in line with the used 3 deposition steps.

Fig. 8 shows cross-sectional SEM images of all thin films deposited onto Mo/SLG substrate. The co-evaporated sample is characterized by a dense structure without a clear definition of grains related to the low substrate temperature used during the co-evaporation process.

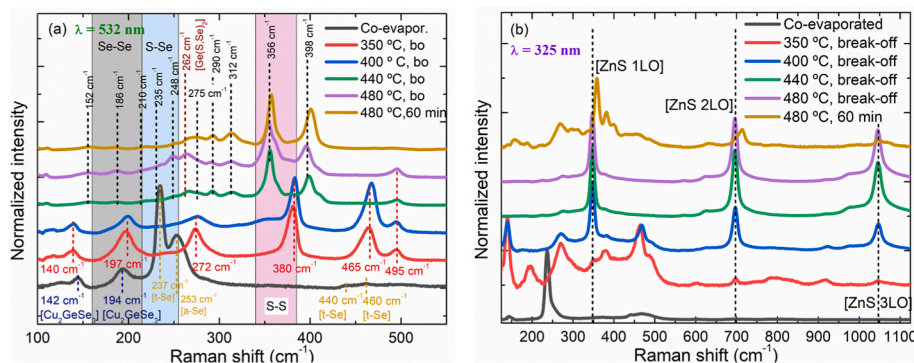


Fig. 6. Raman scattering spectra of all the samples corresponding to Process 1 measured under (a) 532 nm and (b) 325 nm excitation wavelengths.

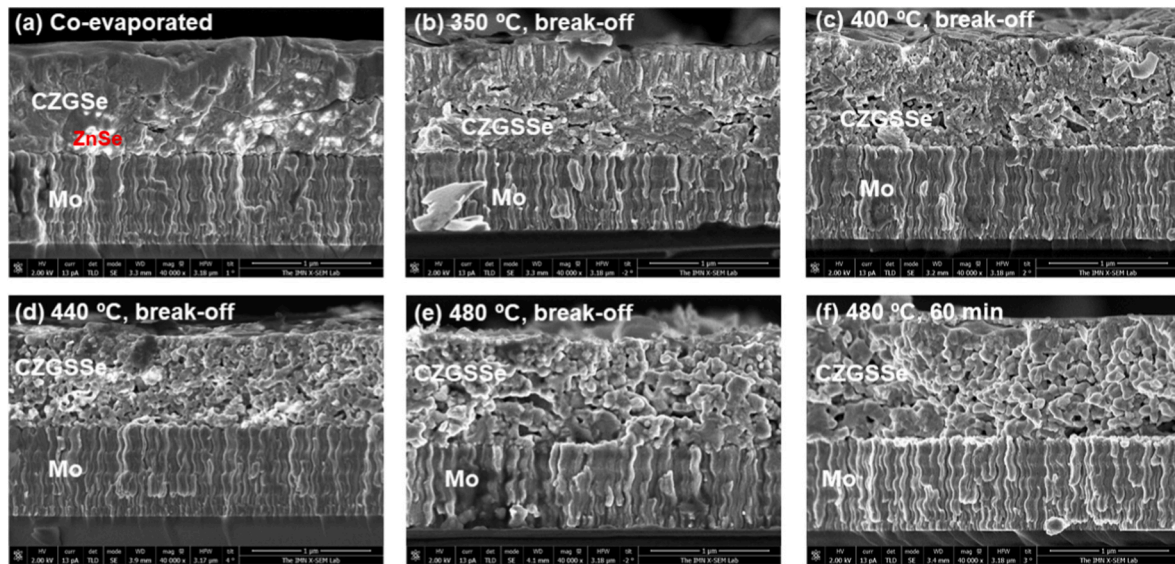


Fig. 8. Cross-sectional SEM images of CZG(S)Se/Mo structure for all the samples of Process 1. After annealing at 480 °C, CZGSe thin film presents a thickness of 1 μm .

However, it is possible to detect some small bright areas which correspond to the ZnSe secondary phase. The sample interrupted at 350 °C during the sulfurization process presents a bilayer structure with very small grains at the back region. After that, all the samples are characterized by a small grain size, being a little bit larger for the sample annealed at the highest temperature (480 °C).

3.2. Investigation of the CZGSe composition on the CZGSe properties

In order to investigate the effect of the composition of the co-evaporated CZGSe thin film on the final CZGSe compound, different co-evaporation processes were performed with different cation ratios.

From the previous break-off experiments, it was concluded that it was necessary to sulfurize the CZGSe thin films at 480 °C for some time to obtain the proper composition and enhance the interdiffusion of elements. Therefore, the following sulfurization processes were performed at 480 °C for 60 min.

Co-evaporation processes 2 and 3 present almost the same [Zn]/[Ge] atomic ratio, but very different Cu concentrations. Therefore, these two experiments allow investigating the role of Cu content of the co-evaporated CZGSe thin film on the S incorporation. As shown in Table 1, the amount of S incorporated into the Cu-poorer CZGSe sample (Process 3) was more than twice of that incorporated into the CZGSe sample coming from Process 2. As we reported previously, Na promotes

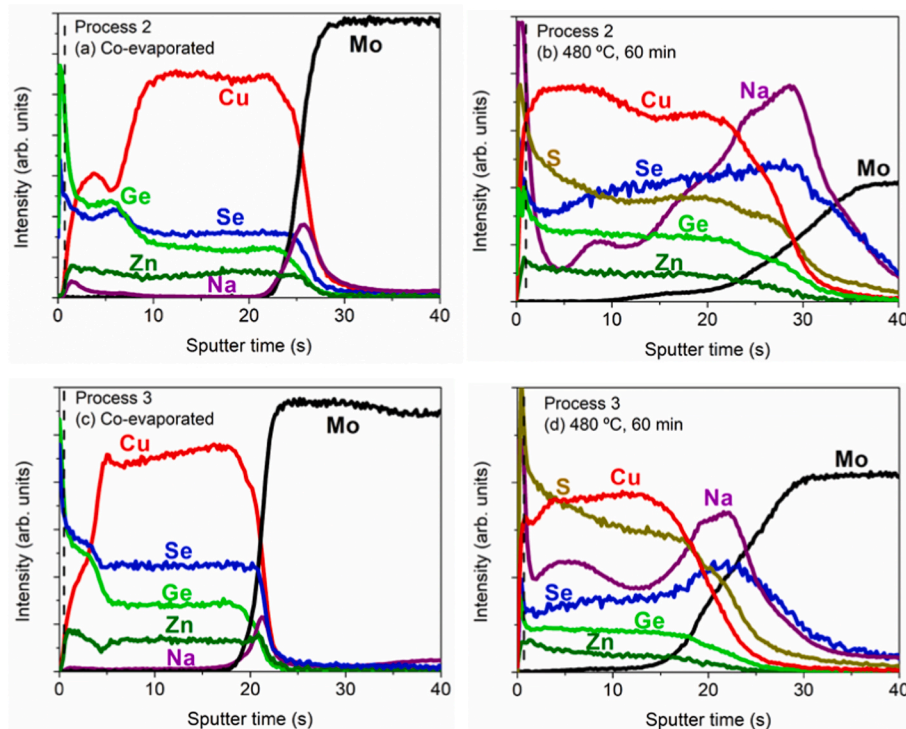


Fig. 9. GD-OES depth profiles of CZG(S)Se/Mo structure for the samples corresponding to the Process 2 (a) and (b), and 3 (c) and (d).

the incorporation of S into the kesterite lattice [20,24], and Na has also affinity for Cu vacancies as in CIGSe [31]. Here, the same nominal amount of Na is used, but, CZGSe samples have been grown with different Cu contents, and, there seems to be an affinity of Cu vacancies to the incorporation of S, which will lead to a higher band gap energy, similar to that observed in CZGSe thin films with higher E_g for lower Cu content [14]. The sulfurization of both samples results in a decrease of Zn content; however, the sulfurization of the co-evaporated sample of Process 2 leads to a significant increase of Ge content similar to what happens for the sample of Process 1.

Fig. 9 displays the elements depth-profiles of samples corresponding to Processes 2 and 3, as measured by GD-OES. As in the case of the co-evaporated samples of Process 1, the elements distribution follows the different stages of the co-evaporation process, presenting a higher Ge, Se and lower Cu, Zn GD-OES signals at the surface regardless of the bulk composition. In both cases, the samples are characterized by a higher Ge and Zn and lower Cu GDO-ES signals near the surface after the sulfurization, with a much higher S and lower Se amount in that region. It is interesting to point out the clear opposite behaviour of Na and Cu after sulfurization, indicating the affinity of Na to Cu vacancies V_{Cu} . The normalized $[S]/([S]+[Se])$ atomic ratio of these sulfurized samples is shown in Fig. 3 b. A continuous increase of the ratio towards the surface is obtained for the sample of Process 3, being the sample of Process 2 more similar to that of Process 1.

GIXRD diffractograms measured at grazing incidence angle of $GI = 4^\circ$ of CZGSSe thin films corresponding to Processes 2 and 3 are shown in Fig. 10. The co-evaporated samples presented the same characteristics as shown in Fig. 5 for Process 1 (not shown here): CZGSe kesterite as the main phase and additional Cu_2Se secondary phase. The presence of ZnSe and Cu_2GeSe_3 cannot be ruled out once again. After the sulfurization of the samples, the main diffraction peaks of CZGSSe are detected together with Mo. Moreover, the sample corresponding to Process 3 presents a diffraction peak at around 15° that can be attributed to a $Ge(S,Se)_2$ secondary phase. This means that the composition of CZGSe is essential for the appearance of secondary phases after sulfurization. A zoom of the 112 Bragg peak of both CZGSSe samples is shown, corroborating a higher incorporation of S into CZGSe lattice for the sulfurized sample corresponding to Process 3, as well as the contribution of two different

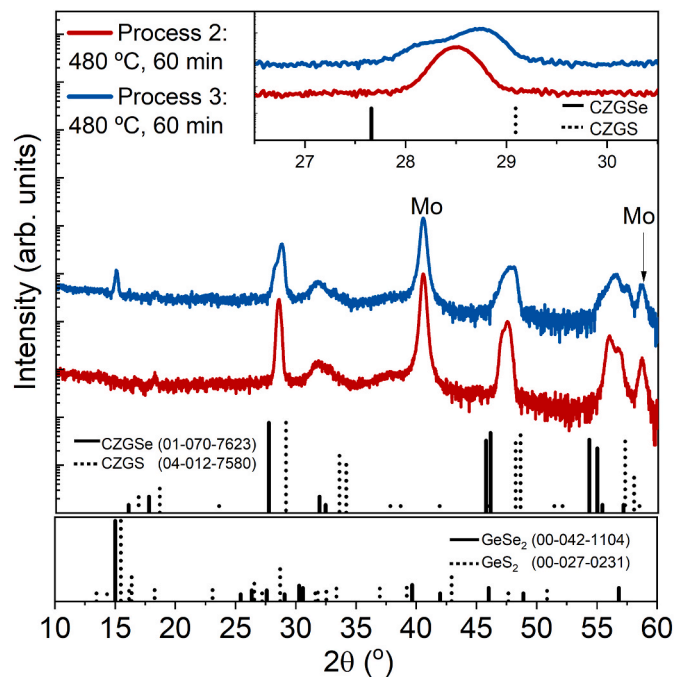


Fig. 10. GIXRD diffraction patterns of CZGSSe after sulfurization coming from Processes 2 and 3. A zoom of 112 Bragg peak is shown.

peaks, being more intense the one corresponding to higher S content in agreement with EDX measurements.

In accordance with the above analysis, the Raman scattering spectra of the sulfurized thin films obtained in the Process 2 and 3 show a significant difference in the anions ratio at the sample surface (Fig. 11). These results show a significantly higher intensity of the Raman peaks related to the Se-Se and S-Se vibration in the sample obtained in the Process 2. In both cases, the presence of the peak related to $Ge(S,Se)_2$ secondary phases can be observed, although, this phase was only detected in the bulk of the thin film of Process 3 by GIXRD analysis. Note, that the Raman spectrum of the as co-evaporated sample was significantly different from the spectrum of the Process 1, and similar to the Process 4, discussed in more detail later on.

Cross-sectional SEM pictures of the samples coming from Processes 2 and 3 before and after sulfurization are displayed in Fig. 12. In these experiments, the kesterite layer is much thinner with a thickness of around 600 nm and 470 nm for samples corresponding to Process 2 and 3 respectively. The co-evaporated samples present a similar structure to that observed for the Process 1 with the inclusion of bright areas corresponding to ZnSe phase in the case of sample 2 related to a slightly higher Zn content. However, the sulfurization results in a much more compact structure of the kesterite-type material with larger grain size, completely different from that obtained in Process 1. Kim et al. [9] reported that $GeSe_2$ li-liquid phase acts as a flux forming large CZTGS grains. Something similar happens here, the CZGSe with higher Ge content leads to larger CZGSSe grain size. Therefore, it can be concluded that the $[Zn]/[Ge]$ ratio of the CZGSe thin film is extremely important for the development of a compact structure and CZGSSe larger grains.

In the case of the co-evaporation process 4, EDX measurements indicate the loss of Ge excess after the sulfurization at $480^\circ C$ for very Ge-rich and very Cu-poor CZGSe thin film which is due to the volatility of Ge at high temperature. In the case of Process 3, a very slight decrease of Ge content was measured after sulfurization. The main common feature between CZGSe from Processes 3 and 4 is the much lower Cu concentration (~ 16 – 17 at % of Cu); and the main difference is the content of Ge. The loss of Ge by the lower Cu content of CZGSe could be a way to avoid the formation of Ge_{Cu} antisite defects; however, a deeper investigation is necessary to understand the relationship between Cu and Ge and their role during the sulfurization process. Some laboratories have observed that CZGSe-based solar cells work better for very Cu-poor composition kesterite layers [32,33]. On the other hand, CZGSe samples from Processes 1 and 2 present very similar Cu concentrations, being the main difference the $[Zn]/[Ge]$ atomic ratio. The higher Ge content or

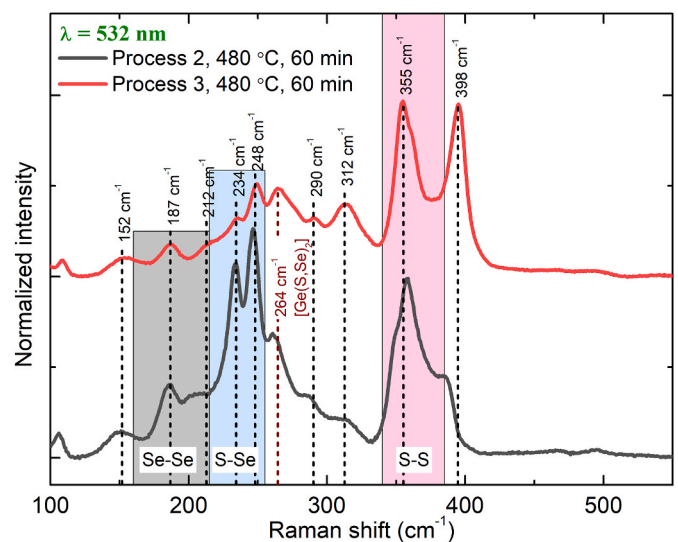


Fig. 11. Raman scattering spectra measured in the surface of the CZGSSe films obtained in Process 2 and 3, after sulfurization.

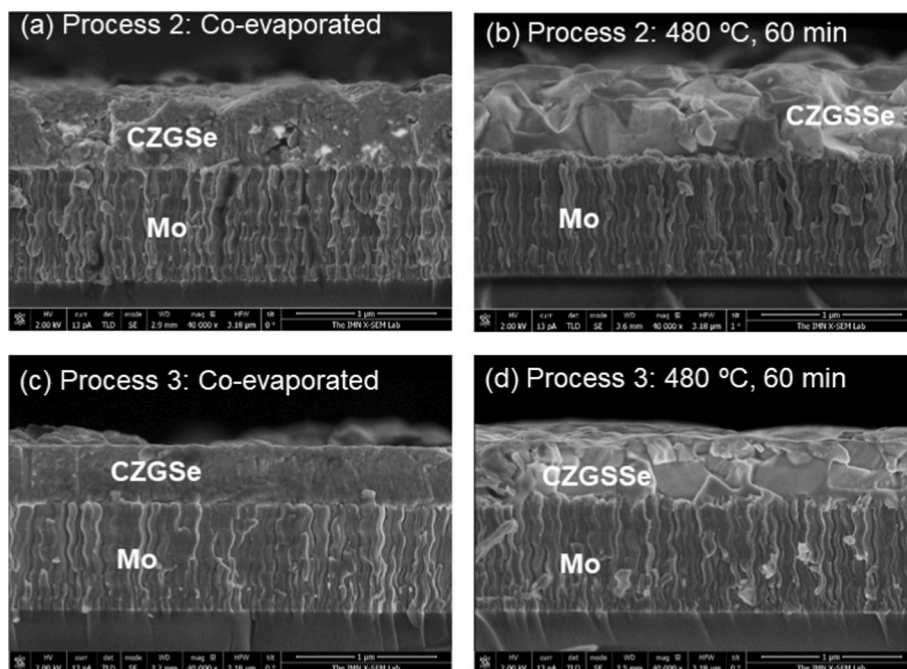


Fig. 12. Cross-sectional SEM pictures of CZG(S)Se/Mo structure corresponding to Process 2 (a) and (b), and 3 (c) and (d). CZGSSe thin films present a thickness of around (b) 550 nm and (d) 450 nm.

lower Zn concentration of Process 2 results in much less incorporation quantity of S into the lattice than in the case of Process 1. A similar behaviour takes place when comparing Processes 3 and 4. Therefore, not only the Cu content is a key parameter for the incorporation of S, but also the [Zn]/[Ge] atomic ratio is relevant for the same amount of Cu; always when the bulk composition is Cu-poor. The sulfurization at 480 °C for 60 min allows for the redistribution and loss of the excessing elements, so that kesterite is the main phase.

As mentioned before, 480 °C is the chosen temperature for the sulfurization process. But, what would occur if some other parameters are modified during the sulfurization? In the samples of Process 4, the effect of the cooling rate and the time at the maximum temperature in the sulfurization process on the properties of the final CZGSSe compound were also investigated. It was observed that neither the time at 480 °C nor the cooling rate significantly affect the bulk composition of the samples. In any case, the optimal composition, Cu-poor and Zn-rich, is achieved to produce efficient solar cells. The question that arises here is whether these parameters will not affect its structural, vibrational and morphological properties to obtain the best kesterite material quality.

Fig. 13 shows GD-OES depth profiles of the samples corresponding to Process 4. Similar to the other CZGSe thin films, the distribution of elements of the co-evaporated sample follows the sequence used during the co-evaporation process. Therefore, the opposite behaviour of the distribution of Cu and Ge can be related more to the low substrate temperature used here, than to the formation of Ge_{Cu} defects because it is independent of the bulk composition of the CZGSe film. The

sulfurization at 480 °C leads to a higher S, Zn and Na GD-OES signal and a lower Cu and Se intensities at the surface region. It is interesting to highlight the different Na depth-profile through the CZGSSe thickness for the three sulfurized samples. A much lower Na GD-OES signal near the back contact is detected for the sample heated at 480 °C for 60 min, indicating an enhanced Na diffusion towards the surface for longer dwell time. Something similar seems to happen for the S in-depth profile. An increase of the S diffusion towards the surface is produced when increasing the time at the higher temperature. As mentioned before, a relationship between the Na and S distribution was already observed in kesterite-type material [20]. Fig. 3c. Shows the $[\text{S}]/([\text{S}] + [\text{Se}])$ intensity ratio depth-profile of these three samples heated at 480 °C. A higher $[\text{S}]/([\text{S}] + [\text{Se}])$ gradient was observed for the sample annealed for longer time. Moreover, the cooling rate has also a slight effect on this gradient. In comparison with the samples heated at 480 °C from Processes 1, 2 and 3, this series of samples present a stronger $[\text{S}]/([\text{S}] + [\text{Se}])$ gradient from half of the CZGSSe film thickness up to the surface.

Fig. 14 displays the GIXRD diffractograms of the samples of Process 4. The co-evaporated sample presents a diffractogram very similar to those of the rest of the CZGSe analyzed in this work. The main diffraction peaks corresponding to the CZGSSe kesterite phase are detected in all the samples after sulfurization. The main difference between them is the appearance of a significant diffraction peak at around 15° corresponding to $\text{Ge}(\text{S},\text{Se})_2$ secondary phase for the samples cooled down at slower rate of 10 °C/min. It seems that there is a competition process between the Ge loss because of the higher temperature and the GeS added during the

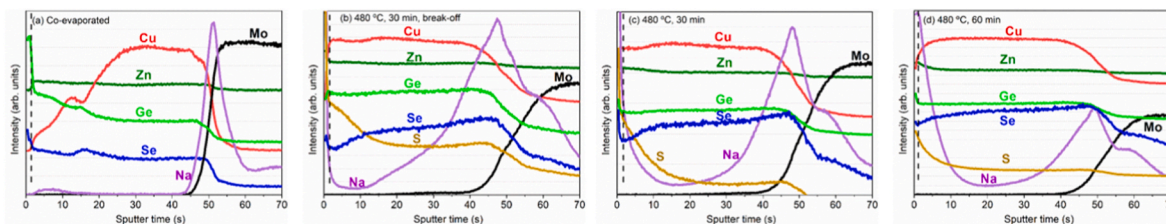


Fig. 13. GD-OES depth profiles of CZG(S)Se/Mo structure for all the samples corresponding to the Process 4. Dashed line represents an artifact because of the sputtering.

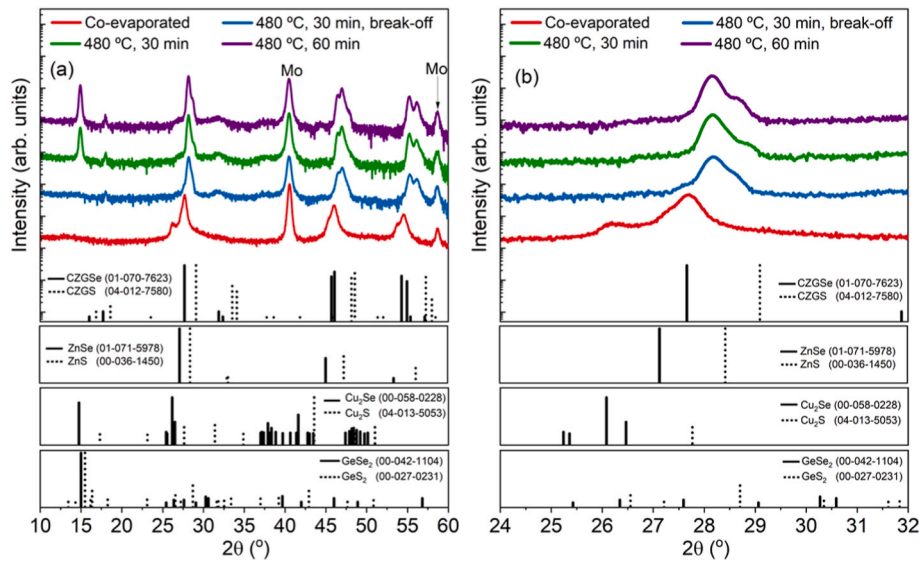


Fig. 14. GIXRD patterns of all the samples investigated corresponding to Process 4.

sulfurization process. These results indicate that a slower cooling rate allows for a higher incorporation of Ge coming from the GeS added in the graphite box used in the sulfurization process, and this extra Ge leads to the formation of $\text{Ge}(\text{S,Se})_2$ secondary phases. Also, the presence of Zn (S,Se) secondary phases cannot be discarded. Fig. 14b. Plots the 112 Bragg peak of all the studied samples corresponding to Process 4. All the sulfurized samples present the contribution of two different peaks due to the non-uniform distribution of $[\text{S}]/([\text{S}] + [\text{Se}])$ ratio.

Fig. 15 displays the Raman scattering measurements of all the samples corresponding to Process 4 using two excitation wavelengths. In the case of the co-evaporated sample Raman peaks corresponding to Se–Se are present close to 200 cm^{-1} (see Fig. 15a.). This peak can be assigned to the main A symmetry peak of CZGSe phase [29]. Here the shoulders at the both sides of the main peak as well as low intensity peaks in the range $230\text{--}310 \text{ cm}^{-1}$ can also be attributed to the kesterite phase, but the crystalline quality is quite low as a result of large bandwidth of all peaks and high overlapping. No secondary phases (including ZnSe phase as follows from the analysis of the Raman spectra measured under 442 nm excitation) or significant lateral inhomogeneity can be noticed in the Raman spectra of this sample. Therefore, despite of the similar GD-OES results showing an increase of the Ge and Se contents at the surface of all as co-evaporated samples, Raman spectroscopy shows that the surface regions of the co-evaporated sample of Process 4 as well as of Processes 2 and 3 are completely different to that of Process 1, and may be related to the uncontrollable precipitation of Se in the evaporation chamber, after the process is finished, although, as mentioned, the pure Se phase can be seen only at the very surface of the thin film from Process 1, and can be

easily removed either by thermal or by chemical treatments.

In accordance with the above results, application of different annealing and/or cooling conditions in the sulfur atmosphere to the CZGSe film from the Process 4 leads to the formation of the CZGSe solid solutions. The Raman spectra show a significant amount of S at the surface, which however decreases in-depth (this can be concluded from the comparison of the spectra measured under 442 and 532 nm excitation wavelengths, not shown here), in well agreement with GD-OES measurements. The in-depth inhomogeneity is also accompanied with the lateral inhomogeneity in all samples (there is a significant variation of the relative intensity of Se–Se peaks from one point to other). From the analysis of the spectra measured under 532 nm excitation wavelength, the $\text{Ge}(\text{S,Se})_2$ secondary phase seems to be present in all samples (peak close to 260 cm^{-1} [12]). While the $\text{Ge}(\text{S,Se})_2$ phase was not detected for the sample with a much faster cooling process by GIXRD; this secondary phase is present at the film surface, and its strong overlapping with the peaks of the main CZGSe phase compromises any quantitative estimation of the amount of this secondary phase. Additionally, analysis of the spectra measured under 325 nm excitation wavelength shows the presence of Zn(S,Se) secondary phase in all samples (see Fig. 15b.) [34].

Cross-sectional SEM pictures of the CZG(S)Se/Mo structure corresponding to Process 4 are displayed in Fig. 16. The sulfurized samples present a compact structure, free of pin-holes with large grains, very different from the co-evaporated sample and the samples of Process 1 but similar to Processes 2 and 3. The samples with a controlled cooling rate present a slight larger grain size and a thin layer of smaller grains at

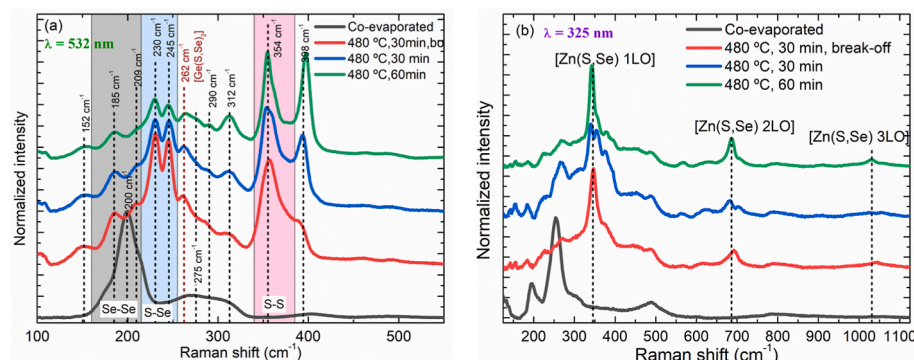


Fig. 15. Raman scattering spectra of all the samples corresponding to Process 4 measured under (a) 532 nm and (b) 325 nm excitation wavelengths.

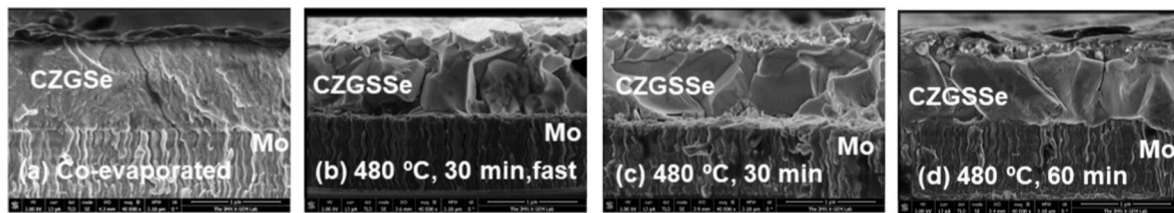


Fig. 16. Cross-sectional SEM pictures of CZG(S)Se/Mo structure corresponding to Process 4. CZGSe thin films present a thickness of around 1 μm .

the surface. Elemental EDX mapping reveals that this thin layer corresponds to the accumulation of Zn (not shown here). These results show the importance of the cooling rate to avoid the segregation of secondary phases. On the other hand, Fig. 16a. Does not show the typical bright areas related to the ZnSe secondary phase, similar to those observed in CZGSe sample obtained in Process 3, presenting these samples a Ge(S, Se)₂ secondary phases in the bulk after annealing at 480 °C for 60 min. Once again, the importance of the composition of CZGSe thin films for the formation of CZGSe compounds is demonstrated here.

The question arising now is, what is the optimal CZGSe composition to produce the higher quality CZGSe compound? There are some common features between the samples investigated despite the different CZGSe starting composition.

- GIXRD diffractograms of all the CZGSe samples show kesterite as the main phase together with Cu₂Se despite the Cu-poor composition of some of the thin films with a Cu concentration of only around 16 at. %. These results indicate that Cu₂Se is a very stable phase at low temperature and needs higher temperature to react with the rest of phases and forms the kesterite-type material independent from the initial amount of Cu, which is clearly observed in the break-off experiments carried out at low temperature (see Figs. 4 and 5).
- The distribution of the elements through the CZGSe thickness is very similar after the sulfurization at 480 °C for 60 min. A much higher S content near the surface is detected in all cases, which is very important in order to increase the V_{OC} of a future solar cell.
- All the samples after the standard sulfurization present CZGSe kesterite as the main phase and secondary phases at the surface. However, proper chemical etching could remove them.

However, the samples also present some clear differences.

- The incorporation of S to form CZGSe compound and the loss of Zn-Ge during the sulfurization process depend on the Cu-content of CZGSe thin films.
- The $[S]/([S]+[Se])$ gradient is different from one sample to another, and this is an important parameter to consider in order to increase the device performance.
- CZGSe thin films with $[Zn]/[Ge] \leq 1$ produce CZGSe films with larger grain size and with a compact structure free of pinholes.
- The standard sulfurization of Ge-rich CZGSe (or $[Zn]/[Ge] < 1$) leads to the segregation of Ge(S,Se)₂ secondary phases in the bulk of CZGSe, which can be avoided with a faster cooling process.

From the structural and morphological point of view, these experiments reveal that it is preferable to co-evaporate Cu-poor CZGSe films with a $[Zn]/[Ge] < 1$, and to perform the sulfurization using a fast cooling rate. By this way, a compact structure with larger grain size of CZGSe and without the segregation of secondary phases in the bulk are expected.

Deeper investigations about the formation of different defects depending on the CZGSe composition will be fundamental to enhance the device performance. These results give us a very important starting point to control the incorporation and distribution of S, which is crucial to increase solar cells efficiency and to use them for different

applications.

4. Conclusions

CZGSe thin films were grown by the sulfurization of co-evaporated CZGSe layers with different cation ratios. First, break-off experiments carried out at different temperatures during the sulfurization process reveal that 440 °C is the key point to develop CZGSe-kesterite type material, and that it is necessary to increase the temperature up to 480 °C for some time to enhance the interdiffusion of the elements. Secondly, the investigation of the influence of the composition of Cu-poor CZGSe samples on the formation of quality CZGSe compounds shows.

1. CZGSe thin films with a minimum Ge content is necessary to assist the growth of CZGSe grains.
2. Cu-poorer CZGSe samples result in a higher S incorporation during the sulfurization process.
3. For CZGSe thin films with the same Cu concentration, the $[Zn]/[Ge]$ atomic ratio dominates the incorporation of S into the CZGSe lattice.
4. The in-depth distribution of $[S]/([S]+[Se])$ ratio depends on the cation's ratios of CZGSe thin films.

These results indicate the importance of controlling the cation ratio of CZGSe to develop high quality CZGSe compounds for efficient devices. The modification of cation ratios allows to control the S incorporation, being very attractive for different applications.

In addition, it was demonstrated that a faster cooling rate during the sulfurization can avoid the segregation of secondary phases as Ge(S,Se)₂, resulting in high quality CZGSe compounds, which could be also relevant to achieve high efficiency solar cells.

CRediT authorship contribution statement

David Palma-Lafuente: Writing – original draft, Visualization, Methodology, Investigation. **Pablo Diez-Silva:** Investigation, Formal analysis. **Victoria Rotaru:** Investigation, Formal analysis. **Tariq Jawhari:** Writing – review & editing, Methodology, Investigation. **Tobias Bertram:** Writing – review & editing, Resources, Methodology. **Pablo Reyes-Figueroa:** Writing – review & editing, Resources, Methodology. **Maxim Guc:** Writing – original draft, Methodology, Investigation, Formal analysis. **José Manuel Merino:** Writing – review & editing, Funding acquisition. **Raquel Caballero:** Writing – original draft, Visualization, Supervision, Resources, Methodology, Investigation, Funding acquisition, Formal analysis, Conceptualization.

Declaration of competing interest

The authors declare that they have no known competing financial interests or personal relationships that could have appeared to influence the work reported in this paper.

Data availability

All the data have been already shown in the manuscript

Acknowledgements

This work was supported by Spanish Ministry of Science, Innovation and Universities Project (CELL2WIN: PID2019-104372RB-C32) and European Project INFINITE-CELL (H2020-MSCA-RISE-2017-777968). DPL acknowledges the financial support from Spanish Ministry of Science and Innovation within FPI Program. MG acknowledges the financial support from Spanish Ministry of Science, Innovation and Universities within the Juan de la Cierva Program (IJC2018-038199-I). Authors from IREC belong to the SEMS (Solar Energy Materials and Systems) Consolidated Research Group of the “Generalitat de Catalunya” (Ref. 2017 SGR 862). The authors acknowledge the service from the MiNa Laboratory at IMN-CSIC, and funding from CM (project S2018/NMT-4291 TEC2SPACE), MINECO (project CSIC13-4E-1794) and European Union (FEDER, FSE).

References

- [1] Y. Gong, Q. Zhu, B. Li, S. Wang, B. Duan, L. Lou, C. Xiang, E. Jedlicka, R. Giridharagopal, Y. Zhou, Q. Dai, W. Yan, S. Chen, Q. Meng, H. Xin, *Nat. Energy* 7 (2022) 966–977.
- [2] M.A. Green, E.D. Dunlop, J. Hohl-Ebinger, M. Yoshita, N. Kopidakis, K. Bothe, D. Hinken, M. Rauer, X. Hao, Solar cell efficiency tables (Version 60), *Prog. Photovoltaics Res. Appl.* 30 (2022) 687–701, <https://doi.org/10.1002/ppp.3595>.
- [3] S. Giraldo, Z. Jehl, M. Placidi, V. Izquierdo-Roca, A. Pérez-Rodríguez, E. Saucedo, Progress and perspectives of thin film kesterite photovoltaic technology: a critical review, *Adv. Mater.* 31 (2019), 1806692, <https://doi.org/10.1002/adma.01806692>.
- [4] M. He, C. Yan, J. Li, M.P. Suryawanshi, J. Kim, M.A. Green, X. Hao, Kesterite solar cells: insights into current strategies and challenges, *Adv. Sci.* 8 (2021), 2004313, <https://doi.org/10.1002/adv.202004313>.
- [5] S. Kim, K.M. Kim, H. Tampo, H. Shibata, S. Niki, Improvement of voltage deficit of Ge-incorporated kesterite solar cell with 12.3 % conversion efficiency, *APEX* 9 (2016), 1202301, <https://doi.org/10.7567/APEX.9.102301>.
- [6] M. Neuschitzer, J. Márquez, S. Giraldo, M. Dimitrievska, M. Placidi, I. Forbes, V. Izquierdo-Roca, A. Pérez-Rodríguez, E. Saucedo, V_{OC} boosting and grain growth enhancing Ge-doping strategy for $Cu_2ZnSnSe_4$ photovoltaic absorbers, *J. Phys. Chem. C* 120 (2016) 9661–9670, <https://doi.org/10.1021/acs.jpcc.6b02315>.
- [7] A.D. Collord, H.W. Hillhouse, Germanium alloyed kesterite solar cells with low voltage deficits, *Chem. Mater.* 28 (2016) 2067–2073, <https://doi.org/10.1021/acs.chemmater.5b04806>.
- [8] L. Choubac, M. Bär, X. Kozina, R. Félix, R.G. Wilks, G. Brammertz, S. Levchenko, L. Arzel, N. Barreau, S. Harel, M. Meuris, B. Vermang, Sn Substitution by Ge: strategies to overcome the open-circuit voltage deficit of kesterite solar cells, *ACS Appl. Energy Mater.* 3 (2020) 5830–5839, <https://doi.org/10.1021/acsaem.0c00763>.
- [9] S. Kim, K.M. Kim, H. Tampo, H. Shibata, K. Matsubara, S. Niki, Ge-incorporated $Cu_2ZnSnSe_4$ thin-film solar cells with efficiency greater than 10, *Sol. Energy Mater. Sol. Cells* 144 (2016) 488–492, <https://doi.org/10.1016/j.solmat.2015.09.039>.
- [10] E. García-Llamas, J.M. Merino, R. Serna, X. Fontané, I.A. Victorov, A. Pérez-Rodríguez, M. León, I.V. Bodnar, V. Izquierdo-Roca, R. Caballero, Wide band-gap tuning $Cu_2ZnSn_{1-x}Ge_xS_4$ single crystals: optical and vibrational properties, *Sol. Energy Mater. Sol. Cells* 158 (2016) 147–153, <https://doi.org/10.1016/j.solmat.2015.12.021>.
- [11] A. Ruiz-Perona, Y. Sánchez, M. Guc, T. Kodalle, M. Placidi, J.M. Merino, F. Cabello, M. García-Pardo, M. León, R. Caballero, The effect of annealing temperature on $Cu_2ZnGeSe_4$ thin films and solar cells grown on transparent substrates, *J. Phys. Mater.* 4 (2021), 034009, <https://doi.org/10.1088/2515-7639/abfa7b>.
- [12] A. Ruiz-Perona, M. Guc, Y. Sánchez, T. Kodalle, J.M. Merino, M. León, R. Caballero, Wide band gap $Cu_2ZnGe(S,Se)_4$ thin films and solar cells: influence of Na content and incorporation method, *Sol. Energy* 226 (2021) 251–259, <https://doi.org/10.1016/j.solener.2021.08.032>.
- [13] T. Schnabel, M. Seboui, E. Ahlswede, Band gap tuning of $Cu_2ZnGeS_xSe_{4-x}$ absorbers for thin-film solar cells, *Energies* 10 (2017) 1813, <https://doi.org/10.3390/en10111813>.
- [14] R. Gunder, J.A. Márquez-Prieto, G. Gurieva, T. Unold, S. Schorr, Structural characterization of off-stoichiometric kesterite-type $Cu_2ZnGeSe_4$ compound semiconductors: from cation distribution to intrinsic point defect density, *CrystEngComm* 20 (2018) 1491–1498, <https://doi.org/10.1039/c7ce02090b>.
- [15] T. Ratz, N.D. Nguyen, G. Brammertz, B. Vermang, J.-Y. Raty, Relevance of Ge incorporation to control the physical behaviour of point defects in kesterite, *J. Mater. Chem.* 10 (2022) 4355–4365, <https://doi.org/10.1039/d1ta09620f>.
- [16] T. Schnabel, M. Seboui, E. Ahlswede, Evaluation of different metal salt solutions for the preparation of solar cells with wide-gap $Cu_2ZnGeS_xSe_{4-x}$ absorbers, *RSC Adv.* 7 (2017) 26–30, <https://doi.org/10.1039/c6ra23068g>.
- [17] T. Schnabel, M. Seboui, A. Bauer, L. Choubac, L. Arzel, S. Harel, N. Barreau, E. Ahlswede, Evaluation of different buffer materials for solar cells with wide-gap $Cu_2ZnGeS_xSe_{4-x}$ absorbers, *RSC Adv.* 7 (2017) 40105–40110, <https://doi.org/10.1039/c7ra06438a>.
- [18] M. Courel, T.G. Sánchez, N.R. Mathews, X. Mathew, Cu_2ZnGeS_4 thin films deposited by thermal evaporation: the impact of Ge concentration on physical properties, *J. Phys. D Appl. Phys.* 51 (2018), 095107, <https://doi.org/10.1088/1361-6463/aaa7db>.
- [19] J. Lee, T. Enkhbat, G. Han, M.H. Sharif, E. Enkhbayar, H. Yoo, J.H. Kim, S. Kim, J. Kim, Over 11% efficient eco-friendly kesterite solar cell: effects of S-enriched surface of $Cu_2ZnSn(S,Se)_4$ absorber and band gap controlled (Zn,Sn)O buffer, *Nano Energy* 78 (2020), 105206, <https://doi.org/10.1016/j.nanoen.2020.105206>.
- [20] A. Ruiz-Perona, G. Gurieva, M. Sun, T. Kodalle, Y. Sánchez, M. Grossberg, J. M. Merino, S. Schorr, M. León, R. Caballero, Routes to develop a [S]/([S]+[Se]) gradient in wide band-gap $Cu_2ZnGe(S,Se)_4$ thin-film solar cells, *J. Alloys Compd.* 868 (2021), 159253, <https://doi.org/10.1016/j.jallcom.2021.159253>.
- [21] J. Andrade-Arvizu, R. Fonoll-Rubio, V. Izquierdo-Roca, I. Becerril-Romero, D. Sylla, P. Vidal-Fuentes, Z.J. Li-Kao, A. Thomere, S. Giraldo, K. Tiwari, S. Resalati, M. Guc, M. Placidi, Controlling the anionic ratio and gradient in kesterite technology, *ACS Appl. Mater. Interfaces* 14 (2022) 1177–1186, <https://doi.org/10.1021/acsaami.1c21507>.
- [22] A. Ruiz-Perona, Y. Sánchez, M. Guc, L. Calvo-Barrio, T. Jawhari, J.M. Merino, M. León, R. Caballero, Influence of Zn excess on compositional, structural and vibrational properties of $Cu_2ZnSn_{0.5}Ge_{0.5}Se_4$ thin films and their effect on solar cell efficiency, *Sol. Energy* 199 (2020) 864–871, <https://doi.org/10.1016/j.solener.2020.02.082>.
- [23] Y.E. Romanyuk, S.G. Haass, S. Giraldo, M. Placidi, D. Tiwari, D.J. Fermin, X. Hao, H. Xin, T. Schnabel, M. Kauk-Kuusik, P. Pistor, S. Lie, L.H. Wong, Doping and alloying of kesterites, *J. Phys. Energy* 1 (2019), 044004, <https://doi.org/10.1088/2515-7655/ab23bc>.
- [24] L. de la Cueva, Y. Sánchez, L. Calvo-Barrio, F. Oliva, V. Izquierdo-Roca, S. Khelifi, T. Bertram, J.M. Merino, M. León, R. Caballero, Sulfurization of co-evaporated $Cu_2ZnSnSe_4$ thin film solar cells: the role of Na, *Sol. Energy Mater. Sol. Cells* 186 (2018) 115–123, <https://doi.org/10.1016/j.solmat.2018.06.015>.
- [25] D. Hironiwa, M. Murata, N. Ashida, Z. Tang, T. Minemoto, Simulation of optimum band-gap grading profile of $Cu_2ZnSn(S,Se)_4$ solar cells with different optical and defect properties, *Jpn. J. Appl. Phys.* 53 (7) (2014), 071201, <https://doi.org/10.7567/JJAP.53.071201>.
- [26] V.V. Poborchii, A.V. Kolobov, K. Tanaka, An in situ Raman study of polarization-dependent photocrystallization in amorphous selenium films, *Appl. Phys. Lett.* 72 (1998) 1167, <https://doi.org/10.1063/1.121002>.
- [27] K. Inoue, O. Matsuda, K. Murase, Raman spectra of tetrahedral vibrations in crystalline germanium dichalcogenides, GeS_2 and $GeSe_2$, in high and low temperature forms, *Solid State Commun.* 79 (1991) 905–910, [https://doi.org/10.1016/0038-1098\(91\)90441-W](https://doi.org/10.1016/0038-1098(91)90441-W).
- [28] G. Marcano, C. Rincón, G. Marín, G.E. Delgado, A.J. Mora, J.L. Herrera-Pérez, J. G. Mendoza-Álvarez, P. Rodríguez, Raman scattering and X-ray diffraction study in Cu_2GeSe_4 , *Solid State Commun.* 146 (2008) 65–68, <https://doi.org/10.1016/j.scc.2008.01.018>.
- [29] M. Dimitrievska, G. Gurieva, H. Xie, A. Carrete, A. Cabot, E. Saucedo, A. Pérez-Rodríguez, S. Schorr, V. Izquierdo-Roca, Raman scattering quantitative analysis of the anion chemical composition in kesterite $Cu_2ZnSn(SxSe_{1-x})_4$ solid solutions, *J. Alloys Compd.* 628 (2015) 464–470, <https://doi.org/10.1016/j.jallcom.2014.12.175>.
- [30] M. Guc, S. Levchenko, V. Izquierdo-Roca, X. Fontané, E. Arushanov, A. Pérez-Rodríguez, Polarized Raman scattering analysis of $Cu_2ZnSnSe_4$ and $Cu_2ZnGeSe_4$ single crystals, *J. Appl. Phys.* 114 (2013), 193514, <https://doi.org/10.1063/1.4830028>.
- [31] R. Caballero, C.A. Kaufmann, V. Efimova, T. Rissom, V. Hoffmann, H.W. Schock, Investigation of Cu(In,Ga)Se₂ thin-film formation during the multi-stage co-evaporation process, *Prog. Photovoltaics Res. Appl.* 21 (2013) 30–46, <https://doi.org/10.1002/ppp.1233>.
- [32] N. Benhaddou, S. Aazou, Y. Sánchez, J. Andrade-Arvizu, I. Becerril-Romero, M. Guc, S. Giraldo, V. Izquierdo-Roca, E. Saucedo, Z. Sekkat, Investigation on limiting factors affecting $Cu_2ZnGeSe_4$ efficiency: effect of annealing conditions and surface treatment, *Sol. Energy Mater. Sol. Cells* 216 (2020), 110701, <https://doi.org/10.1016/j.solmat.2020.110701>.
- [33] I. Anefnaf, S. Aazou, Y. Sánchez, P. Vidal-Fuentes, R. Fonoll-Rubio, K.J. Tiwari, S. Giraldo, Z. Jehl Li-Kao, J. Andrade-Arvizu, M. Guc, E. Saucedo, Z. Sekkat, Insights on the limiting factors of $Cu_2ZnGeSe_4$ based solar cells, *Sol. Energy Mater. Sol. Cells* 227 (2021), 111106, <https://doi.org/10.1016/j.solmat.2021.111106>.
- [34] M. Dimitrievska, H. Xie, A.J. Jackson, X. Fontané, M. Espíndola-Rodríguez, E. Saucedo, A. Pérez-Rodríguez, A. Walsh, V. Izquierdo-Roca, Resonant Raman scattering of ZnS_xSe_{1-x} solid solutions: the role of S and Se electronic states, *Phys. Chem. Chem. Phys.* 18 (2016) 7632–7640, <https://doi.org/10.1039/C5CP04498G>.